Rock Mechanics and Rock Engineering
https://doi.org/10.1007/s00603-023-03664-x

ORIGINAL PAPER

# Chemo-mechanical Alteration of Silicate-Rich Shale Rock after Exposure to $CO_2$-Rich Brine at High Temperature and Pressure

**Ravi Prakash[1] · Samah A. Mahgoub[1] · Sara Abedi[1,2]**

Received: 8 May 2023 / Accepted: 1 November 2023


## Abstract

Owing to their application in rock weathering concerning geostructural stability, enhanced geothermal systems, carbon sequestration, and enhanced oil recovery, the effect of rock–brine–$CO_2$ interactions on the microstructural and mechanical properties of rocks has become a prevalent topic. Understanding the interplay among chemical, microstructural, and mechanical processes is essential to comprehend how they affect rock mechanical alteration. In this study, we examined the effects of chemo-mechanical loading on the microstructural features and mechanical alterations of individual components within the rock. Experiments involved exposing the Permian rock samples to either $CO_2$ or $N_2$-rich brine (a control condition) at a temperature and pressure of 100 °C and 1800 Psi, respectively, for varying duration (14 and 28 days). The ionic strength of the solution was adjusted to 1 M using NaCl. Micro-CT image analysis showed the dissolution of clay- and quartz-rich phases followed by their precipitation. After 14 days, the depth of the outer reacted zone reached roughly 1100 µm, and after 28 days, the depth increased to 1500 µm. Microscale mechanical analysis showed decreased indentation modulus of the clay- and quartz-rich phases after reacting with $CO_2$-rich brine. This decrease in indentation modulus was more than 50% for quartz-rich phases for 28 days of reaction and was lower adjacent to the reacted surface. The decrease in mechanical properties was more pronounced at a distance of 400–600 µm from the reacted surface after 14 days of reaction with $CO_2$-rich brine due to the pore-size controlled solubility phenomenon. Experiments conducted at a greater distance from the reacted surface (approximately 5 mm) revealed a weaker clay–quartz interface, possibly due to the formation of microcracks induced by the swelling of clay particles. Results for the $N_2$ condition show a superficial mechanical alteration of the rock constituents limited to a depth of 200 µm from the reacted surface.

## Highlights

- Study investigates chemo-mechanical and microstructural alteration of silicate-rich shale rock by $CO_2$/ $N_2$-rich brines.
- Dissolution of clay and quartz-rich phases followed by the precipitation of clay and quartz from the transformation of feldspar grains in $CO_2$ condition.
- The modulus of clay- and quartz-rich zones decreased in reacted areas but increased near the surface in $CO_2$ samples.
- $N_2$ condition causes superficial mechanical alteration, minimal dissolution.
- Pore-size-controlled solubility play an important role in the evolution of porosity in the context of rock-fluid interaction.
- Experiments conducted at a greater distance from the reacted surface indicated a weakened clay–quartz interface under $CO_2$ conditions.

✉ Sara Abedi
sara.abedi@tamu.edu

[1] Department of Civil Engineering, Texas A&M University, College Station, TX 77843, USA

[2] Department of Petroleum Engineering, Texas A&M University, College Station, TX 77843, USA

Published online: 01 December 2023

**Keywords** Rock–fluid interaction · $CO_2$ and $N_2$-rich brine · Dissolution and precipitation of secondary mineral phases · Microstructural evolution · Micro-scale mechanical alteration

## 1 Introduction

The impact of rock–brine–$CO_2$ interaction on the microstructural and mechanical properties of rocks has become a prevailing subject because of their numerous applications. These applications include rock weathering concerning the stability of geostructures, enhanced geothermal systems, carbon sequestration, and enhanced oil recovery. Understanding the coupling between chemo-mechanical loading, and mechanical response is pivotal in these applications. Many conventional models consider the effect of rock-fluid interactions structurally uniform and at the bulk-scale. However, recent studies have demonstrated that as a result of porous material and fluid interactions, different zones of reaction form and the alteration of macroscopic mechanical properties depend on the evolution of these reaction zones (Aman et al. 2018; Prakash et al. 2021, 2022). This is due to the coupled and dynamic nature of the rock-fluid interaction, depending on the local pH, spatially varying rock constituents, and chemical composition of the pore fluid. In addition, the reactivity of various rock components varies, and there is a limited understanding of how the rock–brine–$CO_2$ interaction affects the mechanical properties of each rock component within the outer and inner reaction zones.

Previous research has identified typical chemical reactions that occur between rock and $CO_2$-rich brine. These chemical reactions include the transformation of feldspar into diverse mineral assemblages, such as gibbsite, kaolinite, illite, and quartz, depending on physical and chemical conditions (Giles and De Boer 1990; Yuan et al. 2019); the dissolution and formation of carbonates (Arson and Vanorio 2015; Clark and Vanorio 2016; Prakash et al. 2022; Vialle and Vanorio 2011); the oxidation of iron in minerals containing ferromagnesian silicate and sulfides (Earle 2018; Ulmer-Scholle et al. 2014); and the dissolution and formation of silicate and phyllosilicate minerals (Kampman et al. 2016). The chemical reactions mentioned above can result in changes in the microstructure of rock frames, which can cause short-term debonding (STD), long-term debonding (LTD) (Ciantia and Castellanza 2016), the development of microcracks, and alterations to carbonate and silicate cement (Vanorio 2018). When combined with mechanical stress, these chemo-mechanical interactions can lead to additional deformations caused by the compaction and pressure solution (Atkinson 1984; Dewers and Ortoleva 1990; He et al. 2002; Rutter 1983; Tada and Siever 1989; Wawersik et al. 2001).

The above-mentioned experimental studies have been instrumental in guiding investigations and establishing the necessary theoretical framework for modeling and analyzing changes in rock properties (Vanorio 2015). Nonetheless, most of the current rock-physics experimental methods are inadequate for detecting the involved chemo-mechanical interactions when it comes to creating models or interpreting monitoring data. These limitations arise from the nature of conventional measuring techniques, which cannot address the multiphysics and multiscale properties of phenomena that vary over time and space. Overcoming this challenge necessitates the identification of rock characteristics at the microscale where the reactions occur and acknowledging rock heterogeneity as a varying condition.

This study is motivated by the knowledge gaps identified above. The main objective is to investigate how chemo-mechanical loading affects the microstructural characteristics and mechanical alteration of individual components within the rock. Because of the characteristic sizes of various material phases present in rocks (e.g., clay and calcite phases), we employed small-scale testing methods in this study. Specifically, we used nanoindentation for mechanical characterization, scanning electron microscopy-energy dispersive X-ray spectrometry (SEM–EDS) for chemical and compositional evaluation, and micro-CT for microstructural assessment before and after exposing the rocks to $CO_2$-rich brine under high-pressure and temperature conditions. We performed $N_2$ (control condition) experiments for the same duration under the same conditions as the $CO_2$ experiments to distinguish the influence of the pH resulting from the $CO_2$-saturated brine from that of brine. The use of micro-CT coupled with nanoindentation is complementary in this study. Although micro-CT is an effective technique for detecting the evolution of different phases resulting from interactions with reactive brine, it cannot be used to study the evolution of porosity because the average interparticle pore size in the shale rocks is significantly smaller than the micro-CT image resolution. However, at the scale of nanoindentation and EDS performed in this study, the microvolume probed by indentation comprised a porous mineral phase intermixed with organic matter (Abedi et al. 2016a, b; Abedi et al. 2016a, b; Prakash et al. 2021) suggesting that the mechanical responses are functions of the interparticle porosity not accessible by micro-CT imaging. Therefore, using these techniques enabled us to investigate the evolution of material phases and interparticle porosity due to rock and fluid interactions.

## 2 Experimental Methods

### 2.1 Materials and Sample Preparation

We obtained the rock sample used for this analysis from a Permian Formation. The X-ray Diffraction (XRD) analysis provided the mass percentage composition of the Permian rock (Table 1). Major constituents of the samples were quartz, illite, and oligoclase feldspar. Rock eval pyrolysis of the sample revealed an organic content of 5.15%. Before the experiments, sample preparation steps, including cutting, grinding, and polishing, were performed as detailed in Abedi et al. (2016a, b), Martogi and Abedi (2020) and Sharma et al. (2019).

We prepared the rock samples in cuboidal shapes, with two surfaces cut perpendicularly to their bedding direction (referred to as the X1 surface) and the remaining two slides aligned parallel to the bedding (X3 surface).

### 2.2 High-Temperature and High-Pressure Reactions

After preparation, we placed the shale samples in a batch-type Titanium-made Parr dissolution reactor under two conditions at 100 °C. The "$CO_2$" denotes the experiments with $CO_2$ attack, attained by injecting $CO_2$ at 1800 Psi pressure into the reactor. The "$N_2$" denotes the control condition obtained by injecting $N_2$ at 1800 Psi pressure into the reactor. The control condition represents a system with minimal chemical attacks, designed to separate the influences of temperature and pressure from the pH effects induced by $CO_2$-saturated brine. Under each condition, we immersed three samples in brine containing 1 M NaCl and maintained the liquid-to-solid weight ratio at 19. The shale samples were subjected to high-temperature and high-pressure conditions while exposed to brine in the control condition. $CO_2$ (or $N_2$) was injected into the reactor from a pressurized gas cylinder. The pressure was regulated using a syringe pump connected to the reactor, while temperature was maintained via a thermocouple, a temperature controller, and a heating jacket. We maintained the temperature and pressure of 100 °C and 1800 Psi for 2 weeks under $N_2$ and 2 and 4 weeks under $CO_2$ conditions. The reaction duration was long enough for shale samples under $CO_2$ conditions to develop detectable outer reaction zones compared to the $N_2$ samples, but it still had an inner center. After completion, we slowly depressurized the reactor to prevent spalling of the samples. We then cut these samples, grinded and polished the cross-sections for nanoindentation and SEM–EDS.

**Table 1** Mass percent composition of Permian shale before reactions

| Minerals | Proportion (wt %) Unreacted |
|---|---|
| Quartz | 54.59 |
| Illite | 23.31 |
| Feldspar (Albite) | 16.61 |
| Dolomite | 2.54 |
| Pyrite | 1.67 |
| Siderite | 1.27 |

### 2.3 Micro-CT Imaging

The micro-CT image analysis aimed at observing the changes in the mineral and textural compositions of the $CO_2$ and $N_2$ samples. We used the GE Phoenix Nanotom M micro-CT system and operated the X-ray source at a voltage of 90 kV, and the corresponding electric current was 100 µA. We obtained 2800 image slices, and the image resolution achieved was 3 µm; that is, the voxel size is 3 µm. Every voxel of each image slice represents a mineral phase depending on its grayscale value which corresponds to X-ray attenuation coefficient of the mineral and is a function of mineral density, atomic numbers of constituent elements and energy source (Hubbell and Seltzer 1995). The varying X-ray attenuation coefficient is used to segment different constituent minerals. Avizo software package is used to perform image processing and image segmentation (Scientific 2015, 2018; Westenberger 2008). Pre-processing of image stacks and background removal is done following the steps explained in Prakash et al. (2022). Image smoothing or noise removal is performed by applying a nonlocal means filtering algorithm (Buades et al. 2005) using an adaptive-manifold-based approach (Gastal and Oliveira 2012). We used Otsu's automatic segmentation (Otsu 1979) technique to remove the background from the images. Owing to the ultra-low porosity of the shales, the pores were not identifiable at this resolution.

Once we removed the background, the remaining images were segmented based on the sample's mineralogical composition and X-ray attenuation coefficient. At X-ray source voltage of 90 kV, the maximum mineral attenuation coefficient is for pyrite, followed by siderite, dolomite, illite, quartz and oligoclase in descending order. Hence, the highest-intensity (brightest) voxels corresponded to pyrite, whereas the low-intensity (darkest) voxels corresponded to feldspar in the grayscale micro-CT images. Siderite and pyrite had very high mineral attenuation coefficients compared with the other minerals; hence, we clubbed them together during segmentation. Dolomite has a similar attenuation coefficient to quartz, illite, and feldspar and has a small mineral percentage (~ 2.5%). Further, the grain size of dolomite mineral is small; hence it is not possible to identify dolomite grains on micro-CT images with a resolution of 3 µm. Therefore, attempts have not been made to identify

dolomite considering its small grain size, small mineral percentage, and similar attenuation coefficients to other major mineral constituents. In this study, we performed the micro-CT analysis parallel to the bedding direction, consistent with the coupled nanoindentation and SEM–EDS analysis, as explained in the following sections.

### 2.4 Coupled Nanoindentation and SEM–EDS

Nanoindentation is utilized to measure the mechanical properties i.e. indentation modulus and hardness following the procedure detailed in Abedi et al. (2016a, b) and Prakash et al. (2021). We performed grid indentation with 400 indentation points (20 × 20 grid for unreacted and 10 × 40 grid for reacted samples) on a polished cross-section of the reacted sample with a maximum load of 4.8 mN. Performing indentation on the cross-section allowed us to observe the variation in mechanical properties with the depth of the reaction. We obtained the indentation modulus ($M$) and hardness ($H$) from Oliver and Pharr (2004).

$$M = \frac{\sqrt{\pi}}{2}\frac{S}{A_c}, \tag{1}$$

$$H = \frac{P_{max}}{A_c}, \tag{2}$$

where $S = \frac{dP}{dh}$ represents the experimentally measured contact stiffness (initial unloading stiffness) at the maximum load $P_{max}$, and $A_c$ is the projected area of the elastic contact (Abedi et al. 2016a, b; Mashhadian et al. 2018). The latter is a function of the contact depth, $h_c$ and indenter shape. We conducted three sets of indentation grids on the $CO_2$ sample after 14 days of reaction: two were in close proximity to the reacted surface (X1 surface), and one was positioned at a distance of 5 mm from the reacted surface. In addition, we performed two grids after 28 days of reaction with $CO_2$, with one near the reacted surface (X1 surface) and the other at a distance of 5 mm from the reacted surface. One grid was conducted on the $N_2$ sample, and another on the unreacted sample.

EDS scanning aimed to identify the rock surface's elemental map and the chemical composition at each indentation point. We performed EDS microanalysis over the indentation area. We took 30 frames to facilitate the accurate identification of minerals and maintained the dwell time at 3 m.

### 2.5 Multispectral Image Analysis

This analysis aims to obtain a mineralogical map of the rock surface. Once this map represents different minerals (quartz, clay, feldspar, dolomite, and pyrite), we can determine the mineral phase present at each indentation point and the mechanical properties of different minerals at different reaction depths.

The multispectral image analysis performed in this study follows the steps developed by Prakash et al. (2021) and Chancey et al. (2010). We pre-processed individual elemental scans, including removing noise by applying a Gaussian filter and faint signals by applying a threshold. Subsequently, we mathematically merged the three elemental maps using RGB color channels to form a new composite image. Next, we performed unsupervised clustering analysis on this composite image to determine the statistically definable mutually exclusive phases following the steps given by Lydon (2005).

In this study, we obtained multispectral images of quartz-, clay-, and feldspar-rich areas using Si, Al, and Na elemental maps. Using the Ca and S elemental maps, we identified the next multispectral image with dolomite- and pyrite-rich areas. Later, these two images were superimposed to show all minerals together in a single image.

## 3 Results and Discussions

### 3.1 14-Day Rock–Brine–$CO_2$ Interaction

#### 3.1.1 Phase Changes in $CO_2$ Condition After 14 Days of Reaction

Micro-CT imaging was done on a sample post exposure to $CO_2$-rich brine. Micro-CT images were analyzed to study the changes in volume fraction of mineral phases with the depth of reaction. As mentioned, all analyses were performed parallel to the bedding plane to maintain consistency with the nanoindentation and multispectral image analyses. Figure 1 shows one of the grayscale images and its corresponding segmented image, showing clay-, quartz-, feldspar-, and pyrite-rich zones. From the segmented image, clay-rich zones were more abundant close to the reacted surface, confirming the precipitation of clay minerals. In addition, feldspar grains were greatly reduced or absent close to the surface owing to their dissolution, explained by the geochemical reactions of feldspar grains with $CO_2$-rich brine at elevated temperatures and pressures and formation of clay and quartz. Figure 2 shows the volume fractions of the clay-rich, quartz-rich, and feldspar-rich phases as a function of the distance from the exposed surface. Feldspar dissolution and clay precipitation were evident up to 1100 µm. There was also the dissolution of quartz grains near the reacted surface. Quartz has the highest stability against weathering and weathers only after all other silicate minerals have been dissolved. However, increased solubility of quartz minerals has been observed in the presence of organic matter (Bennett and Siegel 1987). Quartz grain dissolution is followed

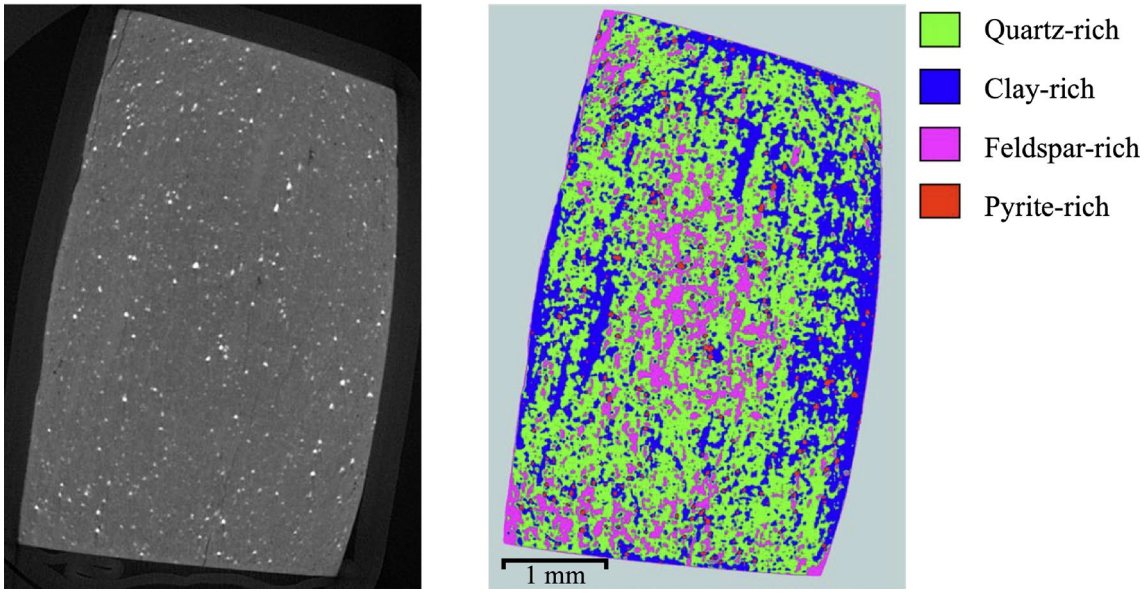


**Fig. 1** A grayscale micro-CT image of Permian shale after exposure to $CO_2$-rich brine (left) along with segmentation results (right)

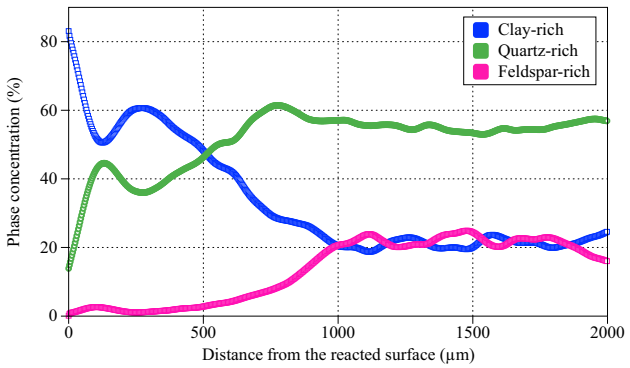


**Fig. 2** Volumetric phase concentration of different mineral phases as a function of distance from reacted surface for Permian shale exposed to $CO_2$-rich brine after 14 days of reaction

by quartz precipitation, resulting from the transformation of feldspar grains in an acidic medium. Feldspar alteration may aid in the sequestration of $CO_2$ by utilizing $H^+$ ions, generating $HCO_3^-$, and buffering the pH of the brine (Yuan et al. 2019).

In summary, the following chemical reactions occur between $CO_2$, brine, and the studied shale sample: First, the dissolution of $CO_2$ in water results in the formation of carbonic acid:

$$CO_2(g) \rightleftharpoons CO_2(aq), \tag{3}$$

$$CO_2(aq) + H_2O \rightleftharpoons H_2CO_3. \tag{4}$$

Subsequently, the generated carbonic acid undergoes dissociation into $HCO_3^-$ and $CO_3^{2-}$, leading to a decrease in the pH of the solution system:

$$H_2CO_3 \rightleftharpoons H^+ + HCO_3^-, \tag{5}$$

$$HCO_3^- \rightleftharpoons H^+ + CO_3^{2-}. \tag{6}$$

The chemical interaction between the solution system and the minerals within the studied shale sample is characterized by the following processes:

$$NaAlSi_3O_8(\text{Albite, Na} - \text{Feldspar}) + 4H^+ \rightleftharpoons 2H_2O + Na^+ + Al^{3+} + 3SiO_2(aq), \tag{7}$$

$$CaMg(CO_3)_2(\text{Dolomite}) + 2H^+ \rightleftharpoons Mg^{2+} + Ca^{2+} + 2HCO_3^-, \tag{8}$$

$$SiO_2 + 2H_2O \rightleftharpoons H_4SiO_4(aq). \tag{9}$$

Dissolution of Na-Feldspar occurs according to Eq. 7. As the reaction progresses with time, the concentration of $Al^{3+}$, $Na^+$ and $SiO_2(aq)$ increases, resulting in the precipitation of secondary minerals. Due to variations in the solute concentrations necessary for saturation (Yuan et al. 2019), secondary minerals have a tendency to form and subsequently dissolve successively within a closed water-feldspar system under a static condition or with low flow rate (Bjorkum and Gjelsvik 1988; Bjørlykke and Aagaard 1992; Bjørlykke and Jahren 2012; Glasmann 1992; Helgeson 1978). Within the diagenetic zone ($T < 200$ °C), as water–rock interactions

progress in a closed Na-feldspar-water system, the probable sequence of secondary minerals is expected to be gibbsite, kaolinite clay, kaolinite + quartz, paragonite + quartz, and finally albite (Bjørlykke and Aagaard 1992). Once the temperature surpasses 200 °C, boehmite can be generated in the initial stage, replacing gibbsite (Fu et al. 2009). However, it's important to clarify that this study did not observe this transition, primarily because the temperature remained at 100 °C. During the 14-day reaction under $CO_2$ condition, our primary observation pertained to the conversion of Na-feldspar into kaolinite clay and kaolinite + quartz.

#### 3.1.2 Chemo-mechanical Changes in $CO_2$ Condition after 14 days of Reaction

Following the procedure explained in Sect. 2.4, grid nanoindentation and SEM–EDS were performed on the cross-sections of the $CO_2$ samples. We performed multispectral image analysis on the EDS elemental maps to obtain a mineralogical map over the indentation grid and determine the mineralogical composition at each indentation point. Figure 3 shows multispectral images of all the major minerals in one of the $CO_2$-reacted Permian shale samples. Evidently, not all indented areas were captured in a single EDS scan. Hence, two multispectral images covered the grid. Using SEM-Back scattered imaging, indentation points were located on clustered mineral maps (black points).

For the $CO_2$ samples, five distinct mineral zones—quartz-, clay-, feldspar-, dolomite-, and pyrite-rich zones—were identified by multispectral image analysis (Fig. 3). The left edge of the first (left) image is the exposed surface, and moving to the right indicates moving away from the reacted surface. We kept the spacing between the indentation columns at 10 µm to a depth of 210 µm from the exposed surface, after which we increased the spacing to 25 µm. We maintained a smaller spacing close to the reacted surface to capture more points in the reacted zone and better understand the changes in the mechanical properties. We created two indentation grids at different locations on the rock, close to the reacted surface, to obtain more confidence in the results. The indentation grids covered the reacted region of the sample till the depth of 710 µm, which according to micro-CT results, is less than the observed reaction depth of 1100 µm.

As shown in Fig. 3, dolomite-rich zones are absent on the left image showing the complete dissolution of dolomite (Eq. 8). Very little or no dolomite was present in the second image until almost half of the image depth. We also performed EDS to capture a larger area and observe the dolomite dissolution in a single image (Fig. 4). As shown in Fig. 4, the dolomite dissolution reaction reaches a depth of ~ 500 µm, after which its concentration gradually increases to reach its value in the unreacted region. In shale rocks with a higher carbonate content, the dissolution of carbonates is followed by precipitation when the concentration of dissolved cations and carbonate anions in the aqueous solution increases (Soong et al. 2002). However, for the present sample, the mass percentage of dolomite was only 2.54%. Therefore, it was not anticipated that the dissolution reaction would result in a sufficiently high concentration of Ca in the solution to trigger the precipitation of carbonate minerals, especially within the 14-day reaction period.

The multispectral image shows that the clay concentration increased close to the reacted surface, as demonstrated by the analysis of the micro-CT images. The clay concentration decreased as we move away from the reacted surface, accompanied by fewer feldspar-rich grains closer to the reacted surface. Another observation is the microstructural change in the pyrite grains close to the reacted surface (Fig. 5). The carbonate mineral siderite has been observed to co-exist with pyrite (Zheng et al. 2017), and the change in

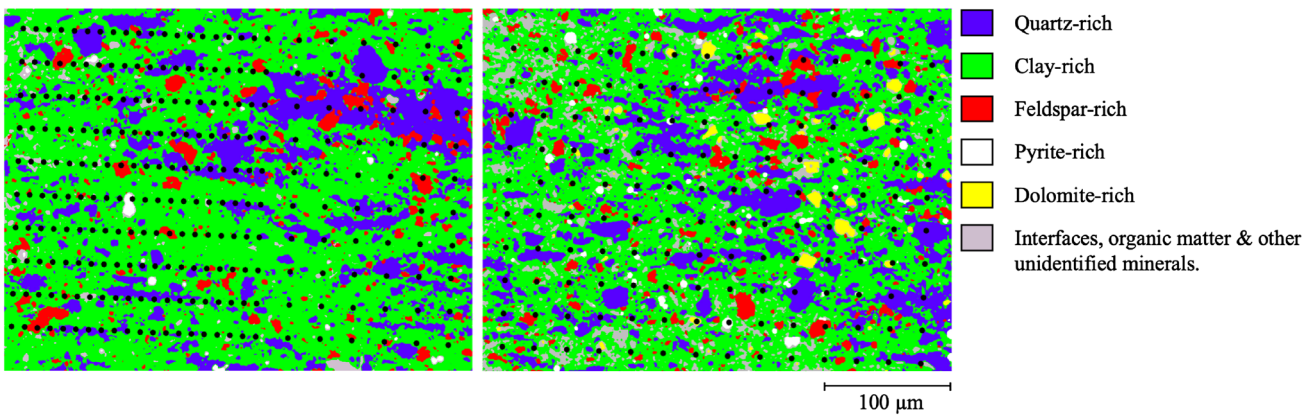


**Fig. 3** Indentation grid pattern superimposed on the multispectral image showing different mineral phases for Permian shale after exposure to $CO_2$-rich brine at high pressure and temperature conditions for 14 days. The left edge of the left image is the exposed surface

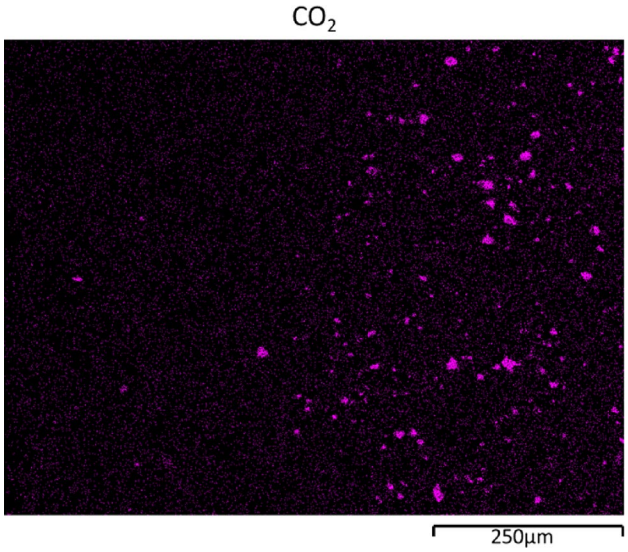


**Fig. 4** Map of Ca in $CO_2$ sample after 14 days of reaction. The left edge is the reacted surface

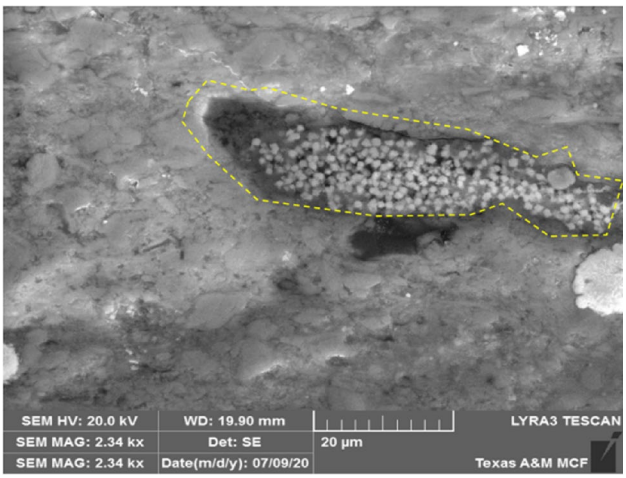


**Fig. 5** SEM image of the Permian sample exposed to $CO_2$-rich brine for 14 days, showing interparticle spaces between grains inside framboidal pyrite

the interparticle spaces between pyrite grains might be the result of the dissolution of siderite.

Figure 6 shows the variation in the indentation modulus of the clay- and quartz-rich phases with the depth of the reaction. Each point on the plot represents the average indentation modulus of a particular mineral within a given column of indentation grid. The solid colored lines represent the data's local polynomial regression fit (Loess fit). The dotted lines indicate the average indentation modulus of the unreacted phases.

As mentioned previously, at the scale of nanoindentation performed in this study, the probed rock microvolume consists of a mineral phase intertwined with porosity and organic matter (Prakash et al. 2021). Consequently, the nanoindentation results were interdependent with respect to the small pore spaces between the mineral grains. For both the clay-rich and quartz-rich zones, we observed a reduction in the modulus in the reacted region concerning the unreacted clay-rich and quartz-rich phases suggesting an increase in the porosity of these phases due to dissolution. This occurred despite the increased concentration of clay-rich zones close to the reacted surface, indicating the high porosity of the precipitated clay particles. However, the modulus of the clay particles increased close to the reacted surface up to a depth of 200 µm compared to the rest of the reacted region. This increased modulus for the clay-rich zones resulted from the excess precipitation of clay minerals, filling up the pores and stiffening the sample close to the reacted surface. We also observe an increase in the modulus of quartz-rich zones in one of the grids near 400 microns of the reacted surface. This increased modulus could be the result from forming amorphous silica (Shao et al. 2010), which has a higher modulus than the reacted quartz grains close to the reacted surface. Presence of amorphous silica cannot be confirmed in EDS maps since it can be confused with quartz. However, for most of the indentation points within the clay-rich and quartz-rich phases, the increased modulus near the reacted surface was still lower than that of the unreacted phases.

For both clay- and quartz-rich phases, the indentation modulus becomes relatively lower at a distance of 400–600 µm away from the reacted surface. The phenomenon known as pore-size-controlled solubility (PCS) (Liu and Jacques 2017; Varzina et al. 2020) can account for this observation, as it often leads to the selective precipitation of minerals in larger pores owing to their lower solubility compared to smaller pores. From a thermodynamic perspective, the PCS follows the same concept as the crystallization pressure in the pores, indicating that the level of supersaturation required for crystal growth increases with increasing confinement pressure. The PCS mechanism can result in the dissolution of minerals in small pores and precipitation into larger pores, similar to Ostwald ripening, a process in which large crystals develop to the detriment of smaller and more soluble crystals (Nabika et al. 2019). The well-known Ostwald–Freundlich equation can also provide an explanation for this mechanism (Correns 1949):

$$\frac{RT}{v_s}\ln S = \frac{2\sigma}{r}, \tag{10}$$

where $R$ is the ideal gas constant, $T$ is the temperature, $v_s$ represents the molar volume of crystals, $S$ denotes the supersaturation index associated with the radius of curvature, $r$, at the crystal–liquid interface, and $\sigma$ is the surface energy of

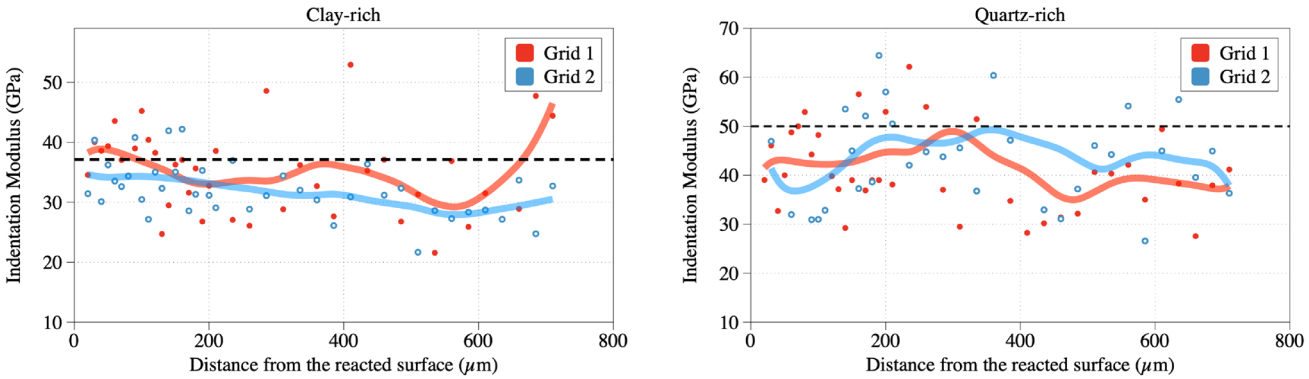


**Fig. 6** Variation of indentation modulus with a depth of reaction for clay- and quartz-rich phases after exposure to $CO_2$-rich brine for 14 days. Each data point represents the average indentation modulus of the clay-rich or quartz-rich phase within a given column of the indentation grid. The solid-colored lines indicate the overall trend, while the dotted lines display the average indentation modulus of the unreacted phases (color figure online)

the crystal. Equation 10 indicates that crystal solubility rises inversely with crystal size, meaning smaller crystals are less stable compared to larger ones. Consequently, crystal precipitation is more likely to initiate within the largest pores. During the initial stages of the reaction, the dissolution of silicate minerals was the dominant interaction mechanism, which led to the increased porosity of the clay- and quartz-rich phases and the formation of secondary clay and quartz minerals resulting from the alteration of feldspar. A portion of the porosity of these phases was occupied by secondary mineral precipitation closer to the reacted surface, thereby increasing the modulus of these phases close to the exposed surface. As the degree of supersaturation decreases with increasing distance from the reacted surface, the precipitation in smaller pores between mineral grains decreases, reaching a minimum at 400–600 µm away from the surface (Fig. 6). This observation is consistent with the PCS mechanism, resulting in a lower modulus of the clay- and quartz-rich phases at a specified distance.

The existence of a softer zone following a stiffer zone in the reacted regions was observed in our previous experiments on different types of shale rocks (Prakash and Abedi 2022; Prakash et al. 2019, 2022), highlighting the significant role that PCS can play in the evolution of porosity in the context of rock-fluid interaction emphasizing the need for further investigation in this area.

In addition to the two indentation grids conducted near the reacted surface, we established an additional indentation grid positioned 5 mm away from the reacted surface. This was done to examine the impact of mechanical damage at a greater distance from the reacted surface. During the 14-day reaction experiment, there was no discernible distinction between the indentation results obtained at a 5 mm distance and those for the unreacted sample. Nevertheless, a noticeable difference emerges in the inner portion of the sample following a 28-day reaction period, which will be explored in greater detail in Sect. 3.3.2.

## 3.2 14-Day Rock-Brine-$N_2$ Interaction

The effect of brine (without $CO_2$) on Permian shale at high temperatures and pressures was studied by injecting $N_2$ into the sample chamber instead of $CO_2$. The brine composition for this reaction was identical to that used for the $CO_2$ injection reaction. After exposing the samples to $N_2$ and brine, micro-CT, nanoindentation, and EDS were performed on the cross-section of the sample, following the same procedure.

### 3.2.1 Phase Changes in the $N_2$ Condition

We similarly performed the micro-CT imaging and segmentation analysis in the X1 direction as explained in the $CO_2$ sample. Figure 7 shows one of a micro-CT images and its corresponding segmented image of the $N_2$ sample. We identified quartz-, clay-, feldspar-, and pyrite-rich phases and the microcracks parallel to the bedding plane. An important observation in the $N_2$ samples is the presence of Al-rich zones close to the reacted surface. We have provided more evidence and explanations for these Al-rich zones in Sect. 3.2.2. These zones were combined with clay-rich phases when analyzing the micro-CT images. Figure 7 shows some deposition/precipitation of clay minerals or Al-rich zones along the X3 surface, which was not visually seen along the X1 surface. Figure 8 shows the volume fraction of the different material phases as a function of the distance from the exposed surface along the X1 surface. We can observe Feldspar and quartz grains dissolution and clay/Al-rich phase precipitation until around 1100 µm. Another noteworthy feature is the gradual transition of the phase concentration in the $N_2$ sample compared to that in the $CO_2$

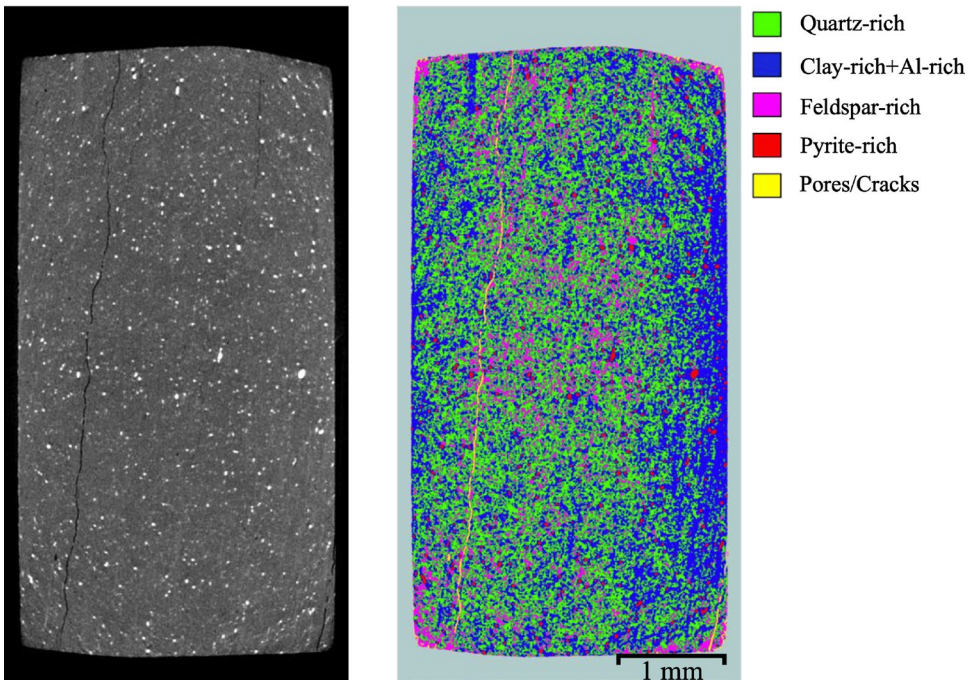


**Fig. 7** A grayscale micro-CT image of Permian shale after exposure to $N_2$-rich brine (left) along with segmentation results (right)

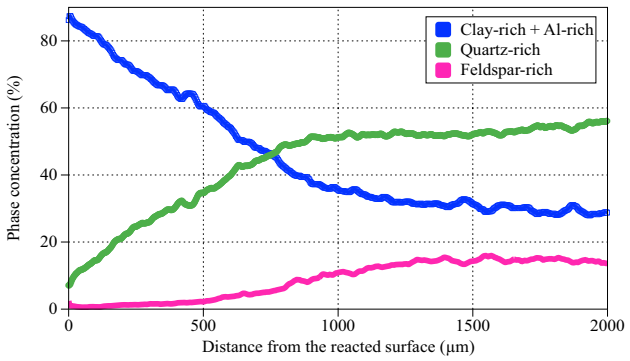


**Fig. 8** Volumetric phase concentration of different mineral phases as a function of distance from reacted surface for Permian shale exposed to $N_2$-rich brine after 14 days of reaction

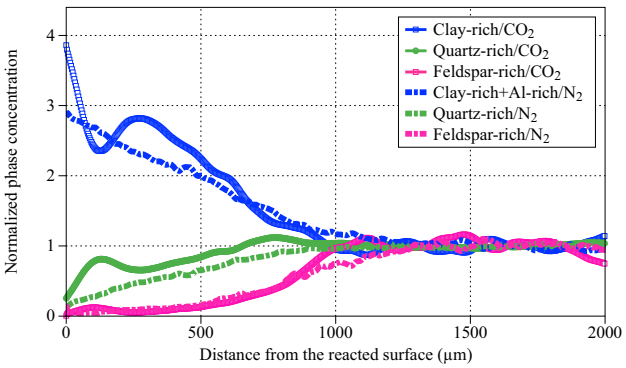


**Fig. 9** Normalized phase concentration of different mineral phases as a function of distance from reacted surface for Permian shale exposed to $CO_2$-rich brine and $N_2$-rich brine after 14 days of reaction

sample. This may be due to the higher reactivity near the exposed surface in an acidic environment than in a neutral environment.

Figure 9 shows the normalized phase concentrations in $CO_2$ and $N_2$ samples as a function of distance from the reacted surface. We normalized the concentration of each mineral phase concerning their concentration in the unreacted region under the same condition ($CO_2$ or $N_2$ condition). The mineral phase evolution in both $N_2$ and $CO_2$ samples exhibits a similar trend. However, it's essential to note that in the $N_2$ condition, Fig. 9 (dashed blue line) combines phase concentrations of clay-rich and Al-rich zones, while the $CO_2$ condition (solid blue line) represents the phase concentration of clay-rich phases exclusively. Figure 9 also illustrates quartz precipitation on top of its dissolution in the $CO_2$ sample. Moreover, quartz and clay precipitation in $CO_2$-reacted samples shows a Liesegang pattern (periodic precipitation) (Nabika et al. 2019).

### 3.2.2 Chemo-mechanical Changes in the $N_2$ Condition

Figure 10 shows two multispectral images of the sample cross-section, with the left edge of the left image being the reacted surface. In addition to the five minerals, we observed Al-rich zones in the sample. No such zones were present in the unreacted samples. Such Al-rich zones are observed under neutral and mildly acidic pH conditions and can be a result of the preferential leaching of Si from feldspar, leaving Al-rich zones in the feldspars (Huang and Keller 1970; Huang and Kiang 1972; Kawano and Tomita 1996; Prakash

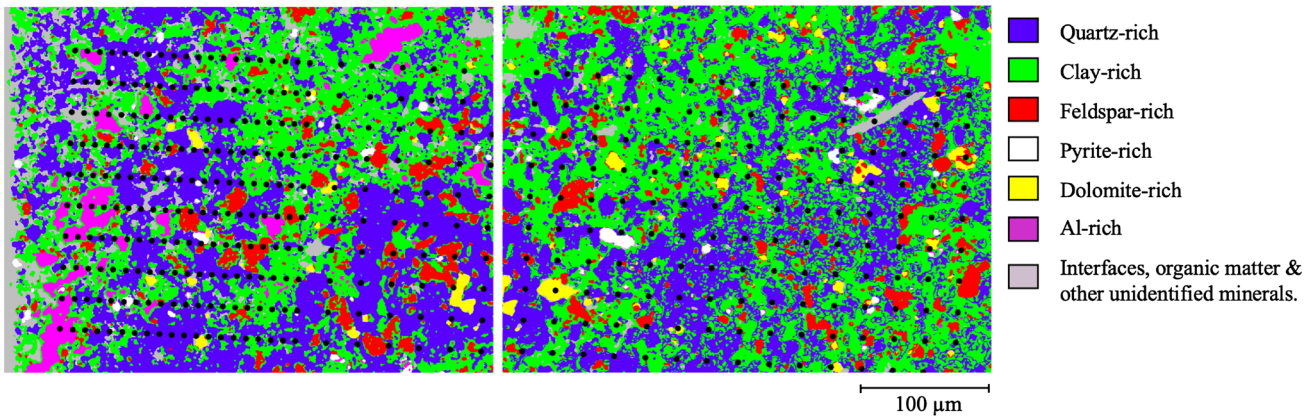


**Fig. 10** Indentation grid pattern superimposed on the multispectral image showing different mineral phases for Permian shale after exposure to $N_2$-rich brine at high pressure and temperature conditions for 14 days. The left edge of the left image is the exposed surface

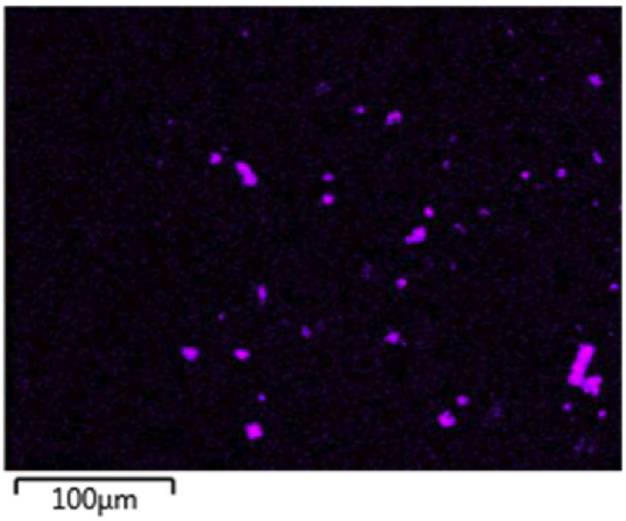


**Fig. 11** Map of Ca in $N_2$ sample after 14 days of reaction. The left edge is the reacted surface

et al. 2021; Reesman and Keller 1965, 1968). As explained in Sect. 3.1.1, these Al-rich zones can be either gibbsite, a weathering product of feldspar, or amorphous $Al(OH)_3$, formed during the early stages of feldspar weathering. Most of these Al-rich zones were very close to the reacted surface. We observed very few grains of feldspar in the vicinity of the areas enriched with Al-rich zones. In the $CO_2$ samples, feldspar dissolution resulted in clay and quartz minerals forming, while in the $N_2$ sample, feldspar weathering resulted in the formation of Al-rich zones very close to the reacted surface and clay minerals (mostly kaolinite). Similar to $CO_2$-reacted sample, this sample also showed dolomite dissolution; however, the depth of the reaction was limited to 200 µm. Figure 11 shows an EDS map of Ca, which represents the dissolution of dolomite. It appears that the impact of the reaction on the mineralogical and compositional properties decreases beyond a depth of 200 µm.

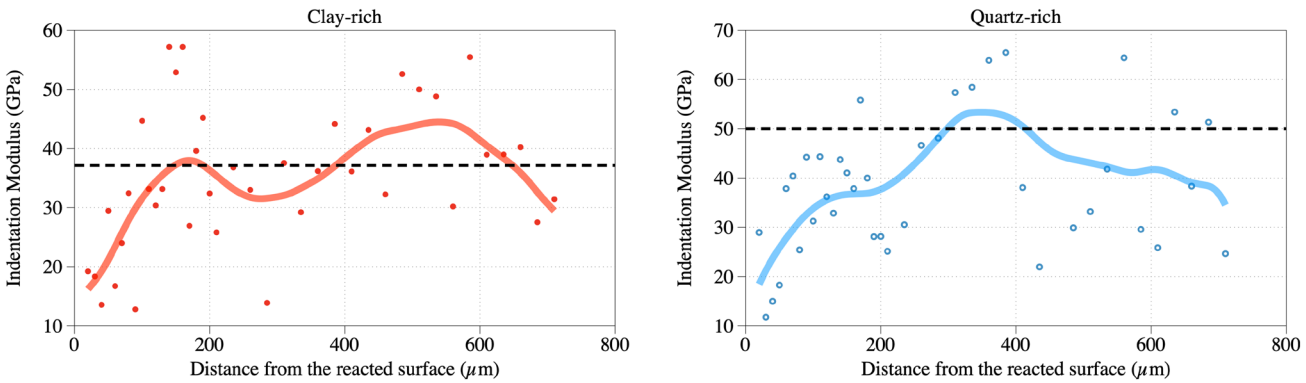


**Fig. 12** Variation of indentation modulus with a depth of reaction for clay- and quartz-rich phases after exposure to $N_2$-rich brine for 14 days. Each data point represents the average indentation modulus of the clay-rich or quartz-rich phase within a given column of the indentation grid. The solid-colored lines indicate the overall trend, while the dotted lines display the average indentation modulus of the unreacted phase (color figure online)

Figure 12 shows the variation in the indentation modulus of the clay- and quartz-rich phases with the depth of the reaction. The solid colored lines represent the data's local polynomial regression fit (Loess fit). The dotted lines indicate the average indentation modulus of the unreacted phases. Unlike the $CO_2$-reacted sample, for this sample, there was a sharp decrease in the modulus close to the exposed surface in both clay-rich and quartz-rich zones. This reduced modulus still has a depth of 200–300 µm, similar to the dissolution depth of dolomite. We can explain this decrease in the modulus by the weathering and washing of grains close to the reacted surface, which made the sample more porous and softer. The decreased moduli of the clay-rich and quartz-rich phases indicate a complete weakening of the sample close to the reacted surface. After this depth of 200–300 µm, the indentation modulus of both quart-rich and clay-rich samples match the unreacted sample. This observation is despite the micro-CT results showing gradual quartz dissolution till the depth of 1100 µm. As mentioned previously, the indentation results were affected by the interparticle pores between the mineral grains. Micro-CT images could not detect these interparticle pores because of their nano- and sub-microscale sizes; however, they affected the indentation results. The shallow depth of alteration of mechanical results may indicate the low intensity of dissolution beyond 200 µm such that the interparticle porosity between grains has not been affected.

A few indentation points were also present in the Al-rich zones. The average indentation modulus was 12.80 GPa, indicating a very weak zone due to feldspar weathering.

## 3.3 28-Day Rock–Brine–$CO_2$ Interaction

We performed rock-fluid interaction experiments on Permian samples exposed to $CO_2$-rich brine for 28 days. After removing the samples from the reactor, all experiments remained the same as 14-day reaction.

### 3.3.1 Phase Changes in $CO_2$ Condition After 28 days of Reaction

Figure 13 shows the volume fractions of the different mineral phases as a function of the distance from the exposed surface. We observed feldspar dissolution up to a depth of 1500 µm. This depth is higher compared to that of the 14-day reacted sample, which was 1100 µm. These reaction depth values suggest that the reaction depth follows Fick's second law, which correlates the depth of the reaction with the square root of time under a constant concentration boundary condition (Fick 1855; Kutchko et al. 2009).

Figure 14 shows the normalized phase concentrations in $CO_2$ samples after 14 and 28 days of reaction as a function of distance from the reacted surface. The concentration of each mineral phase was normalized concerning their concentration in the unreacted region under the same condition (14- or 28-day reaction). The mineral phase evolution of $CO_2$-reacted samples of both 14 and 28 days follows the same trend. However, less clay precipitation is observed on the reacted surface after 28 days of reaction, which aligns with the information provided in Sect. 3.3.1. As delineated by Eq. 7, as the reaction progresses over time, there is an increase in the concentrations of $Al^{3+}$, $Na^+$ and $SiO_2$(aq), resulting in the precipitation of secondary minerals. Within the diagenetic zone ($T < 200$ °C), as water–rock interactions unfold within a closed Na-feldspar-water system, it is anticipated that the sequence of secondary minerals will likely include gibbsite, kaolinite clay, kaolinite + quartz, paragonite + quartz, and ultimately albite, as documented by Bjørlykke and Aagaard (1992). Consequently, there is a notable increase in the dissolution of secondary clay minerals and

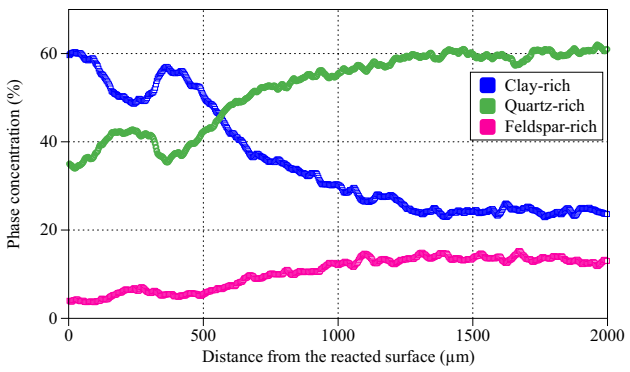


**Fig. 13** Volumetric phase concentration of different mineral phases as a function of distance from reacted surface for Permian shale exposed to $CO_2$-rich brine after 28 days of reaction

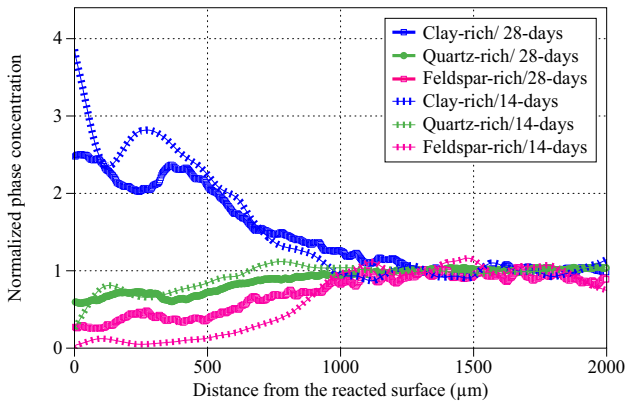


**Fig. 14** Normalized phase concentration of different mineral phases as a function of distance from reacted surface for Permian shale exposed to $CO_2$-rich brine after 14 days and 28 days of reaction

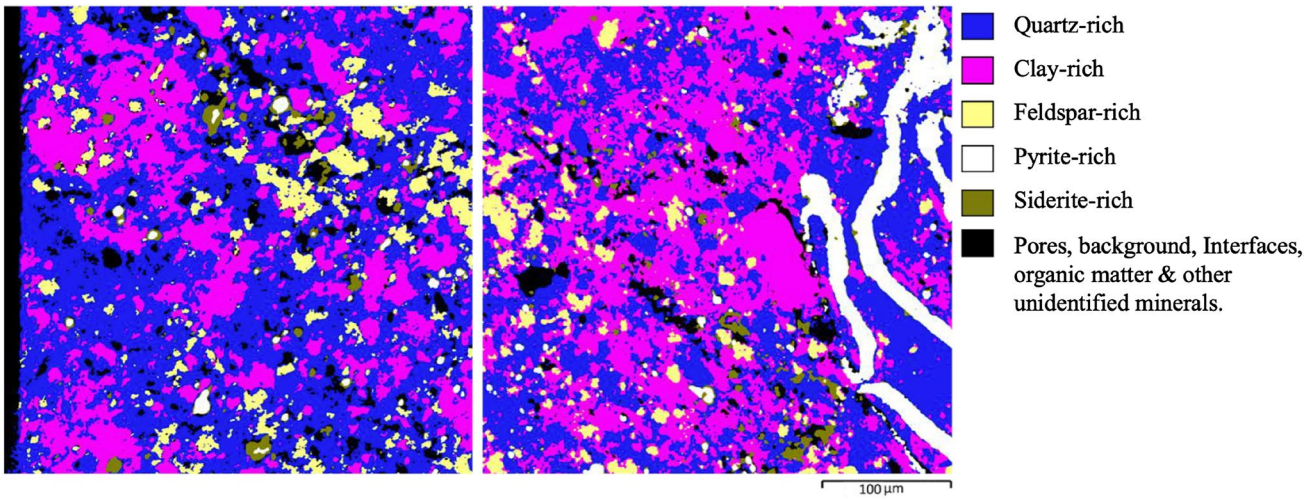


**Fig. 15** Clustered mineral map showing different mineral phases for Permian shale after exposure to $CO_2$-rich brine at high pressure and temperature for 28 days. The left edge of the left image is the exposed surface

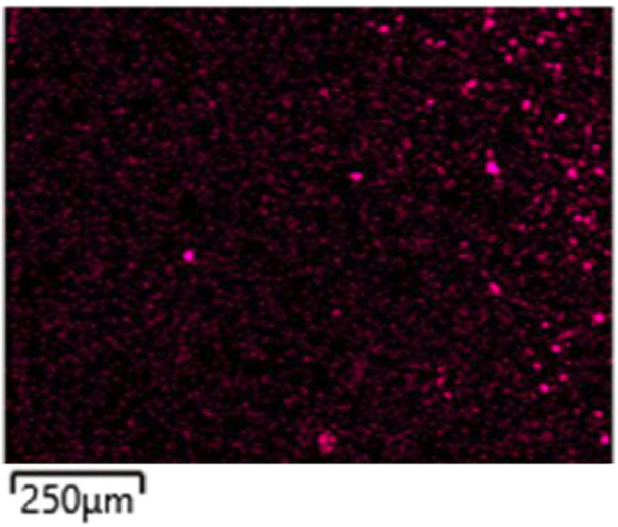


**Fig. 16** Map of Ca in $CO_2$ sample after 28 days of reaction. The left edge is the reacted surface

the precipitation of quartz after 28 days of reaction compared to 14-day reaction.

### 3.3.2 Chemo-mechanical Changes in $CO_2$ Condition After 28 days of Reaction

Figure 15 shows two multispectral images of different minerals µwith different color codes positioned close to the reacted surface. The reacted/exposed surface is situated along the left edge of the left image. This sample had a large strip of pyrite-rich zones towards the end of the reaction zone. This zone did not appear to affect the reactions. Siderite was found in small quantities in this sample. Dolomite-rich zones were completely absent in both images, indicating the dissolution zone to be greater than image sizes of 800 µm combined. We performed a zoomed-out EDS scan at this location to determine the total depth of dolomite dissolution. Figure 16 shows the Ca map, the left edge is the reacted surface, and the field of view for the image is 1200 µm. The EDS scan found the average depth of dolomite dissolution to be approximately 900 µm. For $CO_2$ 14-day and $N_2$ 14-day reactions, the dolomite dissolution depths were 500 µm and 200 µm, respectively (Figs. 4 and 11).

Figure 17 shows variation in the indentation modulus of clay-rich and quartz-rich minerals along the depth of reaction. As with previous indentation graphs, each point on the plot represents the average modulus of each indentation column lying on that particular mineral. The solid colored lines represent the local polynomial regression fit (Loess fit) to the data. The dotted lines show the average of the indentation modulus of the unreacted phases. As expected, for 28 days of reaction, there is a decrease in the modulus of both quartz-rich and clay-rich phases. The trend is similar to 14-day $CO_2$ sample, but this sample is even weaker. The modulus of the quartz-rich phase has decreased by more than 50% except for the first 200 µm, where the modulus is higher than the rest of reacted zone. Clay-rich phases have also shown reduced modulus throughout the indentation grid.

Apart from the indentation grid carried out in close proximity to the reacted surface, we also implemented an additional coupled indentation grid/EDS positioned 5 mm away from the reacted surface. Figure 18 presents the outcomes of the indentation modulus versus indentation hardness for the aforementioned grid, contrasting them with the results acquired from the unreacted sample.

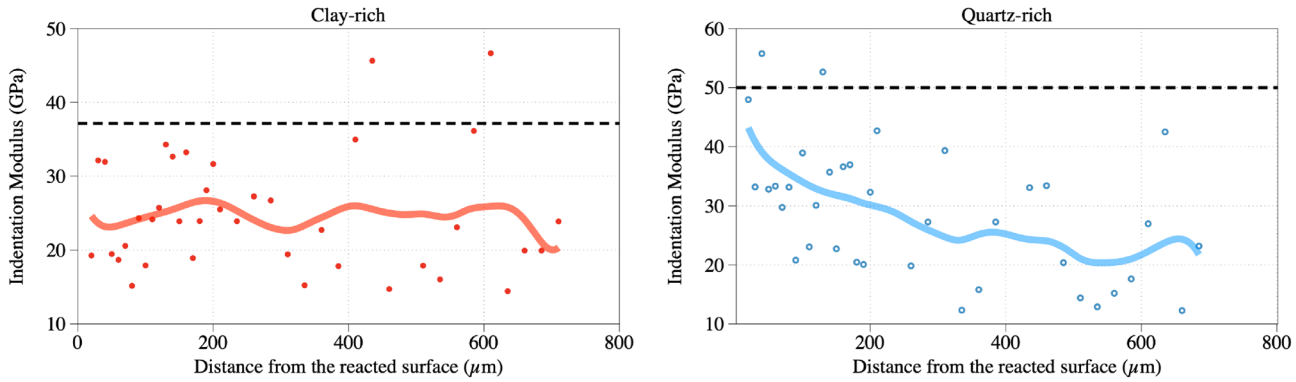


**Fig. 17** Variation of indentation modulus with a depth of reaction for clay- and quartz-rich phases after exposure to $CO_2$-rich brine for 28 days. Each data point represents the average indentation modulus of the clay-rich or quartz-rich phase within a given column of the indentation grid. The solid-colored lines indicate the overall trend, while the dotted lines display the average indentation modulus of the unreacted phases (color figure online)

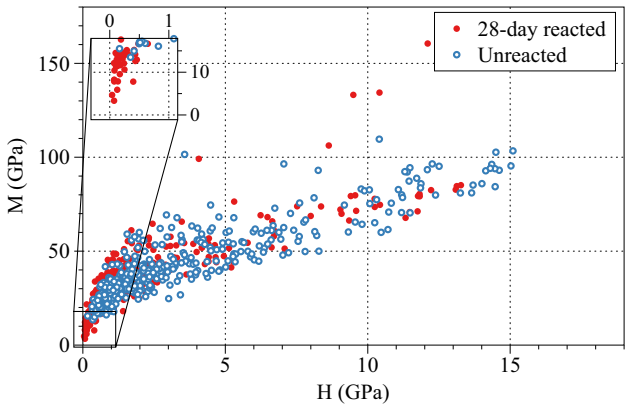


**Fig. 18** Indentation modulus ($M$) versus hardness ($H$) derived from nanoindentation grids conducted on the unreacted and 28-day reacted samples, positioned 5 mm away from the reacted surface. The inset provides a closer look at the indentation points within the 28-day reacted sample, exhibiting lower indentation modulus than the unreacted sample

While the majority of indentation points overlap in the $M$ vs. $H$ plot, however, it's evident that within the 28-day reacted sample, certain indentation points exhibit remarkably low indentation results (modulus < 13 GPa), characteristics not found in the unreacted sample. Figure 19 illustrates a multispectral image of the grid, while Fig. 20 displays color-coded indentation points superimposed on a grayscale multispectral image of the same grid. The colors of the indentation points correspond to the range of their modulus values as indicated by the color bar in the figure. As can be inferred from the Fig. 20, the majority of points exhibiting low modulus values (red dots) are situated at the interface between clay and quartz particles.

This observation could be attributed to the emergence of microcracks at the interface between clay and quartz (Fig. 21), a phenomenon potentially induced by the swelling of clay particles. Prior research has associated the swelling of clay particles with the creation of microcracks resulting from strain incompatibility with non-swelling minerals (Naik Parrikar et al. 2022; Wang et al. 2015, 2017). The coalescence of these microcracks has the potential to give rise to larger cracks, which are noticeable across the depth of the 28-day reacted sample (see Fig. 22). Indeed, a well-defined reaction zone has formed near the reacted surface in the 28-day reacted sample, extending up to a distance of 1500 µm. This zone is marked by significant alterations in mineral composition and micro-mechanical properties. Concurrently, the inner portion of the sample has experienced transformations, including the development of a weakened clay–quartz interface and the appearance of microcracks, which can be attributed to the swelling of clay particles.

## 4 Conclusion

This study investigated shale rock's chemo-mechanical and microstructural alteration due to interaction with $CO_2$- and $N_2$-rich brines under high-pressure and high-temperature conditions. The batch-type dissolution reaction, micro-CT imaging, coupled nanoindentation and EDS, and multispectral image analysis were adapted to measure the samples' physical, mineralogical, and micro-scale chemo-mechanical alterations before and after the reactions. The findings are summarized as follows:

- Results from both coupled nanoindentation and SEM–EDS showed that the reaction under $CO_2$ condition resulted in the dissolution of clay and quartz-rich phases, followed by the precipitation of clay and quartz resulting from the transformation of feldspar grains in an acidic

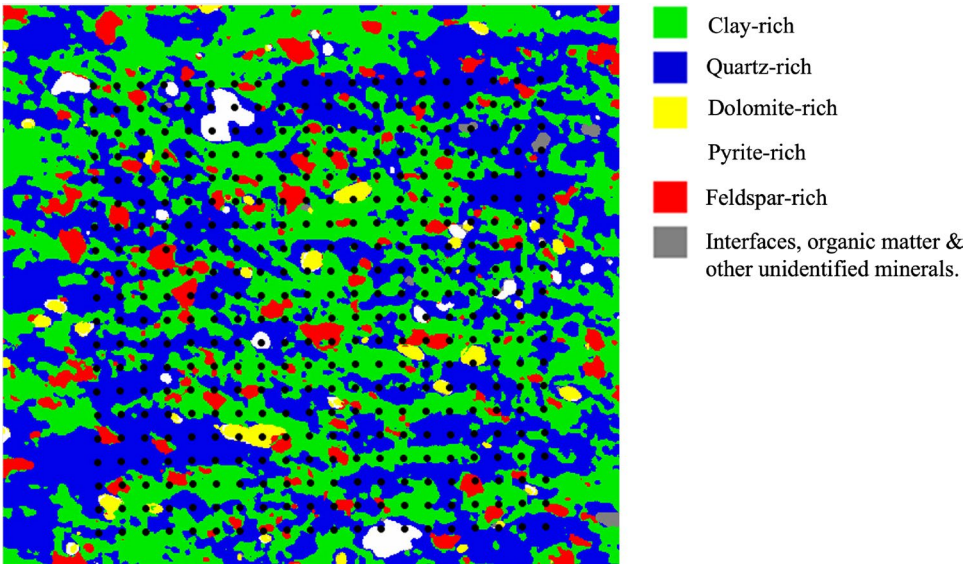


**Fig. 19** Indentation grid pattern superimposed on the multispectral image showing different mineral phases for Permian shale after exposure to $CO_2$-rich brine at high pressure and temperature conditions for 28 days. The indentation grid was positioned 5 mm away from the reacted surface

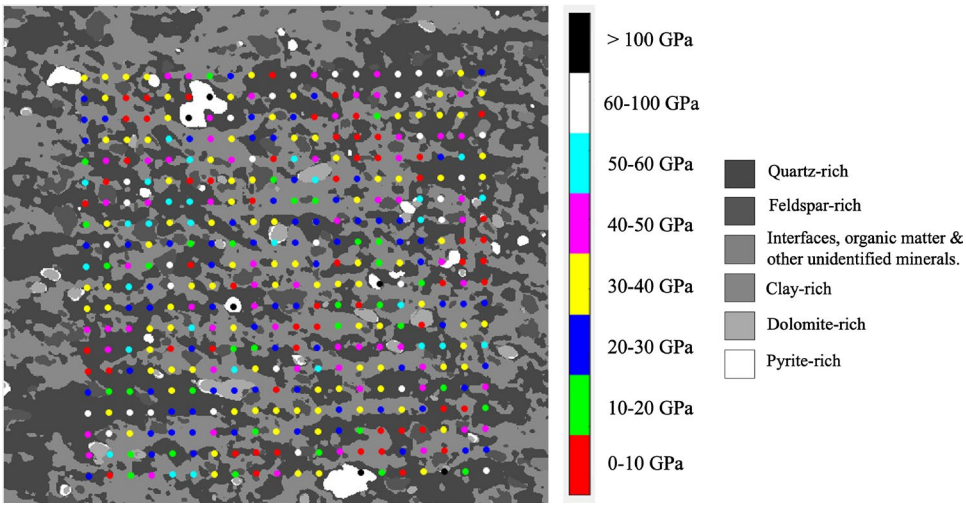


**Fig. 20** Color-coded indentation points superimposed on a gray-scale multispectral image shown in Fig. 19 (color figure online)


**Fig. 21** SEM images showing the formation of microcracks (indicated by the red arrow) at the grains interface within the 28-day reacted sample, positioned 5 mm away from the reaction surface (color figure online)


**Fig. 22** SEM-BSE image displaying the merging of microcracks and the development of a larger crack, evident across the depth of the 28-day reacted sample

medium. The depth of reaction was about 1100 µm after 14 days of reaction under $CO_2$ condition and increased to 1500 after 28 days of reaction in agreement with Fick's second law relationship.

- In both clay- and quartz-rich zones, a decrease in modulus was evident in the reacted region (more than 50% for quartz-rich phases after 28 days of reaction) compared to the unreacted phases rich in clay and quartz. Although the modulus of the reacted clay- and quartz-rich zones was lower than that of the unreacted phases, the formation of amorphous silica and a high concentration of precipitated clay near the reacted surface contributed to an increased modulus in the immediate vicinity of the exposed surface.
- After 14 days of reaction under $CO_2$ conditions, the indentation modulus of both clay- and quartz-rich phases was relatively lower at a distance of 400–600 µm from the reacted surface compared to the rest of the reacted region. This decrease is attributed to the PCS phenomenon, resulting in the selective precipitation of minerals in larger pores owing to their lower solubility compared to smaller pores.
- The samples under $CO_2$ exhibited the creation of clay and quartz minerals owing to the transformation of feldspar grains. Conversely, in the samples under $N_2$, feldspar weathering resulted in the development of Al-rich zones very close to the reacted surface and clay minerals (mostly kaolinite).
- The results of the indentation tests under 14 days of $N_2$ condition indicate that both the clay-rich and quartz-rich phases experienced a superficial mechanical alteration, with a depth of only 200 µm. This implies that there was minimal dissolution beyond this depth such that the porosity between particles remained unaffected.
- Under $CO_2$ conditions, at a greater distance to the reacted surface, the 28-day reacted sample exhibited a weaker interface between clay and quartz particles, which could be attributed to the formation of microcracks in those areas induced by the expansion of clay particles. These microcracks can coalesce and form larger cracks throughout the depth of the sample.

We obtained the findings above by considering pore-scale mechanical and microstructural alterations. They enhanced our understanding of the interaction between rock and reactive brine at the scale of chemical reactions. Further investigation is required to study the effects of changes in the mineralogy, pressure solution, and longer reaction duration on the resulting mechanical alterations of rocks.

**Acknowledgements** The authors acknowledge the use of the Materials Characterization Facility at Texas AandM University. Acknowledgment is made to the National Science Foundation (Grant CMMI-2045242) and to the donors of the American Chemical Society Petroleum Research Fund (PRF 60545-ND9) for supporting this work.

**Funding** This article was funded by National Science Foundation (CMMI-2045242) and American Chemical Society (PRF 60545-ND9).

**Data availability** The datasets produced or analyzed in the present study can be obtained from the corresponding author upon reasonable request.

## Declarations

**Conflict of interest** The authors declare that there is no conflict of interest associated with this publication.

## References

Abedi S, Slim M, Hofmann R, Bryndzia T, Ulm F-J (2016a) Nanochemo-mechanical signature of organic-rich shales: a coupled indentation–EDX analysis. Acta Geotech 11(3):559–572

Abedi S, Slim M, Ulm F-J (2016b) Nanomechanics of organic-rich shales: the role of thermal maturity and organic matter content on texture. Acta Geotech 11(4):775–787

Aman M, Espinoza DN, Ilgen AG, Major JR, Eichhubl P, Dewers TA (2018) CO2-induced chemo-mechanical alteration in reservoir rocks assessed via batch reaction experiments and scratch testing. Greenh Gas Sci Technol 8(1):133–149

Arson C, Vanorio T (2015) Chemomechanical evolution of pore space in carbonate microstructures upon dissolution: linking

pore geometry to bulk elasticity. J Geophys Res Solid Earth 120(10):6878–6894
Atkinson BK (1984) Subcritical crack growth in geological materials. J Geophys Res Solid Earth 89(B6):4077–4114
Bennett P, Siegel D (1987) Increased solubility of quartz in water due to complexing by organic compounds. Nature 326(6114):684–686
Bjorkum PA, Gjelsvik N (1988) An isochemical model for formation of authigenic kaolinite, K-feldspar and illite in sediments. J Sediment Res 58(3):506–511
Bjørlykke K, Aagaard P (1992) Clay minerals in North Sea sandstones. SEPM, Tulsa
Bjørlykke K, Jahren J (2012) Open or closed geochemical systems during diagenesis in sedimentary basins: Constraints on mass transfer during diagenesis and the prediction of porosity in sandstone and carbonate reservoirs. AAPG Bull 96(12):2193–2214
Buades A, Coll B, Morel JM (2005) A non-local algorithm for image denoising. In: 2005 IEEE computer society conference on computer vision and pattern recognition (CVPR'05)
Chancey RT, Stutzman P, Juenger MC, Fowler DW (2010) Comprehensive phase characterization of crystalline and amorphous phases of a Class F fly ash. Cem Concr Res 40(1):146–156
Ciantia MO, Castellanza R (2016) Modelling weathering effects on the mechanical behaviour of rocks. Eur J Environ Civ Eng 20(9):1054–1082
Clark AC, Vanorio T (2016) The rock physics and geochemistry of carbonates exposed to reactive brines. J Geophys Res Solid Earth 121(3):1497–1513
Correns CW (1949) Growth and dissolution of crystals under linear pressure. Discuss Faraday Soc 5:267–271
Dewers T, Ortoleva P (1990) A coupled reaction/transport/mechanical model for intergranular pressure solution, stylolites, and differential compaction and cementation in clean sandstones. Geochim Cosmochim Acta 54(6):1609–1625
Earle S (2018) Physical geology
Fick AV (1855) On liquid diffusion. Lond Edinb Dublin Philos Mag J Sci 10(63):30–39
Fu Q, Lu P, Konishi H, Dilmore R, Xu H, Seyfried W Jr, Zhu C (2009) Coupled alkali-feldspar dissolution and secondary mineral precipitation in batch systems: 1. New experiments at 200 C and 300 bars. Chem Geol 258(3–4):125–135
Gastal ES, Oliveira MM (2012) Adaptive manifolds for real-time high-dimensional filtering. ACM Trans Gr (TOG) 31(4):1–13
Giles M, De Boer R (1990) Origin and significance of redistributional secondary porosity. Mar Pet Geol 7(4):378–397
Glasmann JR (1992) The fate of feldspar in Brent Group reservoirs, North Sea: a regional synthesis of diagenesis in shallow, intermediate, and deep burial environments. Geol Soc Lond Spec Publ 61(1):329–350
He W, Hajash A, Sparks D (2002) A model for porosity evolution during creep compaction of sandstones. Earth Planet Sci Lett 197(3–4):237–244
Helgeson HC (1978) Summary and critique of the thermodynamic properties of rock-forming minerals. Am J Sci A 278:1–229
Huang W, Keller W (1970) Dissolution of rock-forming silicate minerals in organic acids: simulated first-stage weathering of fresh mineral surfaces. Am Mineral J Earth Planet Mater 55(11–12):2076–2094
Huang W, Kiang W (1972) Laboratory dissolution of plagioclase feldspars in water and organic acids at room temperature. Am Mineral J Earth Planet Mater 57(11–12):1849–1859
Hubbell JH, Seltzer SM (1995) Tables of X-ray mass attenuation coefficients and mass energy-absorption coefficients 1 keV to 20 MeV for elements Z= 1 to 92 and 48 additional substances of dosimetric interest. National Inst. of Standards and Technology-PL, Gaithersburg
Kampman N, Busch A, Bertier P, Snippe J, Hangx S, Pipich V, Di Z, Rother G, Harrington J, Evans JP (2016) Observational evidence confirms modelling of the long-term integrity of CO 2-reservoir caprocks. Nat Commun 7:12268
Kawano M, Tomita K (1996) Amorphous aluminum hydroxide formed at the earliest weathering stages of K-feldspar. Clays Clay Miner 44(5):672–676
Kutchko BG, Strazisar BR, Huerta N, Lowry GV, Dzombak DA, Thaulow N (2009) CO2 reaction with hydrated class H well cement under geologic sequestration conditions: Effects of flyash admixtures. Environ Sci Technol 43(10):3947–3952
Liu S, Jacques D (2017) Coupled reactive transport model study of pore size effects on solubility during cement-bicarbonate water interaction. Chem Geol 466:588–599
Lydon J (2005) The measurement of the modal mineralogy of rocks from SEM imagery: the use of Multispec© and ImageJ freeware. Geol Surv Can Open File 4941:37
Martogi D, Abedi S (2020) Microscale approximation of the elastic mechanical properties of randomly oriented rock cuttings. Acta Geotech 15(12):3511–3524
Mashhadian M, Verde A, Sharma P, Abedi S (2018) Assessing mechanical properties of organic matter in shales: results from coupled nanoindentation/SEM-EDX and micromechanical modeling. J Petrol Sci Eng 165:313–324
Nabika H, Itatani M, Lagzi I (2019) Pattern formation in precipitation reactions: the Liesegang phenomenon. Langmuir 36(2):481–497
Naik Parrikar P, Mokhtari M, Saidzade A (2022) Measurement of deformation heterogeneity during shale swelling using digital image correlation. J Energy Res Technol 144(6):063002
Oliver WC, Pharr GM (2004) Measurement of hardness and elastic modulus by instrumented indentation: advances in understanding and refinements to methodology. J Mater Res 19(1):3–20
Otsu N (1979) A threshold selection method from gray-level histograms. IEEE Trans Syst Man Cybern 9(1):62–66
Prakash R, Abedi S (2022) Computational modeling of creep behavior in shales induced by fluid-rock interaction. In: 56th US rock mechanics/geomechanics symposium
Prakash R, Kana Nguene P, Seers T, Noshadravan A, Abedi S (2019) Chemo-mechanical investigation of CO2-fluid-rock interaction in CO2 storage and CO2-EOR processes in unconventional reservoirs. In: 53rd US rock mechanics/geomechanics symposium
Prakash R, Nguene PCK, Benoit D, Henkel K, Abedi S (2021) Assessment of local phase to mechanical response link: application to the chemo-mechanical identification of rock phases subjected to reactive environments. J Nat Gas Sci Eng 89:103857
Prakash R, Nguene PCK, Noshadravan A, Abedi S (2022) Chemical reactions of carbonate-rich mudstones with aqueous CO2 and their impacts on rock's local microstructural and chemo-mechanical properties. J Nat Gas Sci Eng 103:104587
Reesman A, Keller W (1965) Calculation of apparent standard free energies of formation of six rock-forming silicate minerals from solubility data. Am Mineral J Earth Planet Mater 50(10):1729–1739
Reesman A, Keller W (1968) Aqueous solubility studies of high-alumina and clay minerals. American Mineralogist: Journal of Earth and Planetary Materials 53(5–6):929–942
Rutter E (1983) Pressure solution in nature, theory and experiment. J Geol Soc 140(5):725–740
Scientific TF (2015) Avizo Software 9.0 release notes. Thermo Fisher Scientific, Hillsboro
Scientific TF (2018) Amira-Avizo Software. Thermo Scientific™ Amira-Avizo Software
Shao H, Ray JR, Jun Y-S (2010) Dissolution and precipitation of clay minerals under geologic CO2 sequestration conditions:

CO2−brine−phlogopite interactions. Environ Sci Technol 44(15):5999–6005
Sharma P, Prakash R, Abedi S (2019) Effect of temperature on nano- and microscale creep properties of organic-rich shales. J Petrol Sci Eng 175:375–388
Soong Y, Jones R, Hedges S, Knoer J, Thompson R, Harrison D, Baltrus J (2002) CO2 sequestration using brines. In: Abstracts of papers of the american chemical society
Tada R, Siever R (1989) Pressure solution during diagenesis. Annu Rev Earth Planet Sci 17:89
Ulmer-Scholle DS, Scholle PA, Schieber J, Raine RJ (2014) Diagenesis: iron sulfide, oxide & hydroxide cements, pp 347–360
Vanorio T (2015) Recent advances in time-lapse, laboratory rock physics for the characterization and monitoring of fluid-rock interactions. Geophysics 80(2):WA49–WA59
Vanorio T (2018) Challenges and recent advances in rock physics. In: International geophysical conference, Beijing, China, 24–27 April 2018
Varzina A, Cizer Ö, Yu L, Liu S, Jacques D, Perko J (2020) A new concept for pore-scale precipitation-dissolution modelling in a lattice Boltzmann framework–application to portlandite carbonation. Appl Geochem 123:104786
Vialle S, Vanorio T (2011) Laboratory measurements of elastic properties of carbonate rocks during injection of reactive CO2-saturated water. Geophys Res Lett 38(1)
Wang L, Bornert M, Yang D, Héripré E, Chanchole S, Halphen B, Pouya A, Caldemaison D (2015) Microstructural insight into the nonlinear swelling of argillaceous rocks. Eng Geol 193:435–444
Wang L, Zhang G, Hallais S, Tanguy A, Yang D (2017) Swelling of shales: a multiscale experimental investigation. Energy Fuels 31(10):10442–10451
Wawersik WR, Rudnicki JW, Dove P, Harris J, Logan JM, Pyrak-Nolte L, Orr FM, Ortoleva PJ, Richter F, Warpinski NR (2001) Terrestrial sequestration of CO2: an assessment of research needs. Advances in geophysics, vol 43. Elsevier, New York, p 97
Westenberger P (2008) AVIZO-3D visualization framework. In: Geoinformatics conference
Yuan G, Cao Y, Schulz H-M, Hao F, Gluyas J, Liu K, Yang T, Wang Y, Xi K, Li F (2019) A review of feldspar alteration and its geological significance in sedimentary basins: From shallow aquifers to deep hydrocarbon reservoirs. Earth Sci Rev 191:114–140
Zheng X, Wang Z, Wang L, Xu Y, Liu J (2017) Mineralogical and geochemical compositions of the lopingian coals and carbonaceous rocks in the Shugentian coalfield, Yunnan, China: With emphasis on Fe-bearing minerals in a continental-marine transitional environment. Minerals 7(9):170